

Impact of TRMM Data on a Low-Latency, High-Resolution Precipitation Algorithm for Flash-Flood Forecasting

ROBERT J. KULIGOWSKI

NOAA/NESDIS/Center for Satellite Applications and Research, Camp Springs, Maryland

YAPING LI

I. M. Systems Group, Inc., NOAA/NESDIS/Center for Satellite Applications and Research, Camp Springs, Maryland

YU ZHANG

NOAA/NWS/Office of Hydrologic Development, Silver Spring, Maryland

(Manuscript received 12 April 2012, in final form 20 December 2012)

ABSTRACT

Data from the Tropical Rainfall Measuring Mission (TRMM) have made great contributions to hydrometeorology from both a science and an operations standpoint. However, direct application of TRMM data to short-fuse hydrologic forecasting has been challenging because of the data refresh and latency issues inherent in an instrument in low Earth orbit (LEO). To evaluate their potential impact on low-latency satellite rainfall estimates, rain rates from both the TRMM Microwave Imager (TMI) and precipitation radar (PR) were ingested into a multisensor framework that calibrates high-refresh, low-latency IR brightness temperature data from geostationary platforms against the more accurate but low-refresh, higher-latency rainfall rates available from microwave (MW) instruments on board LEO platforms. The TRMM data were used in two ways: to bias adjust the other MW data sources to match the distribution of the TMI rain rates, and directly alongside the MW rain rates in the calibration dataset. The results showed a significant reduction in false alarms and also a significant reduction in bias for those pixels for which rainfall was correctly detected. The MW bias adjustment was found to have much greater impact than the direct use of the TMI and PR rain rates in the calibration data, but this is not surprising since the latter represented perhaps only 10% of the calibration dataset.

1. Introduction

Flash floods remain one of the deadliest and most costly natural disasters worldwide, particularly in regions without the means to invest in high-density rain gauge and radar networks to provide vital information on rainfall. Satellites offer a low-cost alternative source of rainfall information that also overcomes some of the limitations of gauge and radar data—particularly by providing coverage over rugged terrain and large bodies of water.

However, the use of satellite data for retrieving rainfall is challenging at the space and time scales required for flash-flood forecasting. Microwave (MW)-based estimates of rainfall are generally more accurate than those from

infrared (IR) techniques; however, MW instruments are restricted to low Earth orbit and thus are not able to provide the latency and data refresh rate required for forecasting flood conditions in small basins. Consequently, while data from the Tropical Rainfall Measuring Mission (TRMM) have been widely used and have had tremendous benefit from both a science and an operational perspective, direct application to short-term, low-latency events such as flash floods has been a challenge. IR data from geostationary satellites possess the requisite brief latency and frequent data refresh, but the relationship between cloud-top properties from IR data to rainfall rates at the surface is much less direct than that between the bulk cloud ice and water sensed in the MW frequencies and surface rainfall.

To address this issue, numerous investigators have developed schemes for combining the frequency of the visible–IR retrievals with the accuracy of the MW retrievals. Many of these techniques have relied on using the MW data as a calibration standard for a statistical

Corresponding author address: Robert J. Kuligowski, NCWCP ERA2, 5830 University Research Ct., 2nd Fl., Office 2828, College Park, MD 20740-3818.
E-mail: bob.kuligowski@noaa.gov

IR-driven algorithm based on regression (e.g., Miller et al. 2001), artificial neural networks (e.g., Hsu et al. 1997; Bellerby et al. 2000; Hong et al. 2004), or simple distribution matching (e.g., Turk et al. 2003; Huffman et al. 2007) to develop the IR rainfall model. All of these methods are affected by the limited information content of the IR window band relative to the MW instrument; a different approach has been taken by the Climate Prediction Center (CPC) morphing technique (CMORPH; Joyce and Xie 2011) and Global Satellite Mapping of Precipitation (GSMaP; Ushio et al. 2009), in which the IR data are used only as the basis for interpolating MW measurements between successive overpasses. An intercomparison by the International Precipitation Working Group (IPWG; Ebert et al. 2007) has shown CMORPH to be the most accurate of the algorithms compared. However, CMORPH and many of the other algorithms mentioned here are either not run in real time or are not run with sufficiently low data latency for flash-flood applications.

In this paper, the potential impact of TRMM data on short-response forecasting is evaluated by incorporating the data into an algorithm called the self-calibrating multivariate precipitation retrieval (SCaMPR; Kuligowski 2002) that is specifically designed to produce estimates with very low data latency (~ 20 min) in real time. It should be noted that the focus of this study is not to evaluate SCaMPR relative to other algorithms, but rather to use SCaMPR to evaluate the potential impact of TRMM data within a framework that would allow it to be used to impact low-latency estimates of rainfall.

This paper serves as a companion to Zhang et al. (2013) by providing a detailed description of the modifications to the SCaMPR algorithm and exploring the reasons for the observed impacts on algorithm performance over the conterminous United States (CONUS), whereas the Zhang et al. (2013) paper is more strongly focused on the relative hydrologic utility of SCaMPR versus interpolated gauge-only products on an areal average basis for drainage basins in Texas and Louisiana.

The second section of this paper will briefly review the original SCaMPR algorithm and describe modifications that have been made since the 2002 paper. The third section will describe efforts to incorporate TRMM data into the algorithm, and section 4 will describe the impact of this work. The paper will close with a summary and introduction of future work on the algorithm.

2. Methodology

a. Original version of SCaMPR

The original version of SCaMPR is described in detail in Kuligowski (2002). In brief, it is an algorithm for retrieving rainfall rate from geostationary IR data that is

dynamically calibrated based on continually updated relationships between IR-derived inputs and rainfall rates from the Special Sensor Microwave Imager (SSM/I) from the Fleet Numerical Meteorology and Oceanography Center (FNMOC; Ferraro 1997). The algorithm originally selected from a set of eight predictors that are derived from Geostationary Operational Environmental Satellite (GOES) imager data: brightness temperature bands 3 (6.5 or 6.7 μm), 4 (10.7 μm), and 5 (12.0 μm —*GOES-11* and earlier) or 6 (13.3 μm —*GOES-12* and later); the brightness temperature difference (BTD) between bands 3 and 4; IR-derived rainfall rates from the Auto-Estimator (Vicente et al. 1998, 2002; Scofield 2001) and the GOES multispectral rainfall algorithm (GMSRA; Ba and Gruber 2001); and the G_t and S texture parameters that originated in the convective-stratiform technique (CST) of Adler and Negri (1988):

$$G_t = T_{\text{avg}} - T_{\text{min}} \quad \text{and} \quad (1)$$

$$S = 0.568(T_{\text{min}} - 217 \text{ K}), \quad (2)$$

where T_{min} is the minimum value of the 10.7- μm channel brightness temperature $T_{10.7}$ within the surrounding 5×5 pixel area and T_{avg} is the mean of the six nearest pixels (four along the scan line and two across the scan). The value of G_t increases with the degree of cloud texture, and S is a threshold value that allows greater degrees of texture for colder clouds (Adler and Negri 1988). During the calibration process, the GOES predictors are aggregated onto the MW footprints for consistency.

The calibration and retrieval processes are divided into two separate steps, the first of which is rain/no-rain discrimination. Discriminant analysis is used to select from the potential rain/no-rain predictors and to calibrate the optimal linear combination (if there are two or more) using the Heidke skill score (HSS):

$$\text{HSS} = \frac{2(c_1c_4 - c_2c_3)}{(c_1 + c_2)(c_2 + c_4) + (c_3 + c_4)(c_1 + c_3)}, \quad (3)$$

where c_1 is the number of correct no-rain detections (dry estimate and dry observation), c_2 is the number of false alarms (wet estimate and dry observation), c_3 is the number of missed events (dry estimate and wet observation), and c_4 is the number of correct rain detections (wet estimate and wet observation). Since the HSS can sometimes have an optimal value but a highly biased result, the threshold rain/no-rain value for each predictor set is adjusted to ensure a bias of less than 5%. The algorithm can select up to two predictors—higher numbers of predictors have been tested but not shown to have any beneficial impact.

The second calibration step is rainfall-rate retrieval. Since the algorithm performs rain/no-rain discrimination as a first step, only those pixels with MW rain rates exceeding 0.25 mm h^{-1} are used in the rate calibration. The relationship between IR brightness temperature and rainfall rate is highly nonlinear (e.g., Fig. 1 in Vicente et al. 1998), so a supplementary set of eight predictors is created by regressing each of them in log–log space to derive the coefficients for a power-law transformation (i.e., $y = ax^b$). Stepwise forward multiple linear regression is then used to select the predictors to be used in the retrieval. As with rain/no-rain discrimination, only two predictors are selected because additional predictors were not shown to be beneficial.

The resulting equations for rain/no-rain discrimination and rain-rate retrieval are applied to subsequent GOES images, and the calibration is updated whenever new MW rain rates become available; they replace the oldest MW rain rates in the calibration dataset. Thus, the calibration will be updated 3–6 times per day on average. It should be emphasized, however, that the calibration update and the rainfall-rate retrieval are independent processes and the latency of the calibrating MW rainfall rates has no effect on the latency of the SCA-MPR rainfall rates; the SCA-MPR rainfall rates are produced with a latency of roughly 20 min using the most recent calibration.

b. SCA-MPR modifications

SCA-MPR has been running in real time at National Environmental Satellite, Data, and Information Service/Center for Satellite Applications and Research (NESDIS/STAR) since November 2004 but is different from the version presented in Kuligowski (2002). The Auto-Estimator and GMSRA are no longer used as predictors, and the BTDs between GOES imager bands 3 and 5/6 and between bands 4 and 5/6 have been added to the predictor set. Also, Advanced Microwave Sounding Unit-B (AMSU-B)/Microwave Humidity Sounder (MHS) rain rates from the Microwave Surface and Precipitation Products System (MSPPS; Ferraro et al. 2005; Vila et al. 2007) supplement the SSM/I rain rates from FNMOC. In an attempt to homogenize the distributions of the rain rates in the two datasets, the SSM/I rain rates are multiplied by 0.85 and the rain/no-rain threshold used for the AMSU-B/MHS is 2.0 mm instead of 0.25 mm . Since the AMSU-B/MHS is a cross-track scanner, all footprints with a scan angle exceeding 40° are ignored to minimize the variation in footprint size. [Note that as the Defense Meteorological Satellite Program (DMSP) satellites prior to *F-16* have been retired, SSM/I data have not been replaced with Special Sensor Microwave Imager/Sounder (SSM/I/S) data in the control version of

SCA-MPR described here because of concerns about biases in the operational FNMOC SSM/I/S rainfall rates caused by directly substituting the 91-GHz radiances for 85-GHz radiances in their retrievals.]

The spatial coverage of the real-time version of SCA-MPR is much larger (20° – 60°N , 135° – 60°W) than the sample regions in Kuligowski (2002), and it was determined that the same calibration was not optimal over the entire area. Consequently, the coverage area was divided into overlapping $15^\circ \times 15^\circ$ regions (10° of overlap in both directions) such that each pixel effectively had nine computed SCA-MPR rain rates (one for each of the $15^\circ \times 15^\circ$ regions that overlapped the pixel) that were averaged into a single value using an inverse distance-weighting scheme (distance from the pixel of interest to the center of each $15^\circ \times 15^\circ$ box).

The Kuligowski (2002) version of SCA-MPR used a fixed time period for calibration, but experiments showed that during extended periods of dry weather or very light rain the calibration became optimized for little or no rain and performed very poorly when heavier precipitation occurred. To maintain the representation of significant precipitation in the training dataset, the size of the training dataset is fixed at 500 pixels with rain rates of at least 2.5 mm h^{-1} plus all of the nonraining pixels from the same time periods. Thus, the length of the training dataset and the number of data points in it are allowed to vary in time such that the number of pixels with significant rainfall rates is held constant to maintain a more consistent calibration for significant rainfall rates.

c. Incorporation of TRMM data

The introduction of TRMM data to SCA-MPR was performed for a retrospective dataset covering 2000–07 and the geographic region of 10° – 50°N and 120° – 80°W . This allowed the study to be centered on the West Gulf River Forecast Center (WGRFC) as part of a larger study. The WGRFC region was chosen since that office routinely uses satellite quantitative precipitation estimation (QPE) to supplement radar data south of the Rio Grande.

The TRMM data were added to SCA-MPR in two steps. The first was to use the TRMM Microwave Imager (TMI) 2A12, version 6, product rainfall rates (Kummerow et al. 2001; McCollum and Ferraro 2003) to bias adjust the SSM/I and AMSU-B/MHS data prior to ingest into SCA-MPR. The approach used was similar to that in Joyce and Xie (2011), where histograms from simultaneous overpasses of TMI (which had been aggregated to 15-km resolution) and the other sensors over a 1-month period were used to construct lookup tables (LUTs) that matched the SSM/I or AMSU-B/MHS rain rate at a given fractile to the TMI rain rate at the same fractile. Applying the LUTs to the SSM/I and AMSU-B/MHS

rain rates would result in distributions identical to that of the TMI. The same LUTs were used for land and ocean; no land–ocean separation was performed.

The second step was to add the TMI and the precipitation radar (PR) 2A25, version 6, product (Iguchi et al. 2009) rainfall rates to the target dataset. The TMI data were added only in those portions of the TMI swath not covered by the PR to avoid having two different calibration targets for the IR data within the PR swath. The PR was chosen over the TMI since it is generally more accurate (it serves as the TMI calibration target). To ensure consistency, these data were aggregated to the footprint size of the SSM/I and AMSU-B/MHS (15 km) prior to ingest.

3. Results

a. Overall impacts of TRMM data

The results were evaluated by comparing the hourly SCaMPR totals with the hourly stage IV (Lin and Mitchell 2005) totals produced at the National Centers for Environmental Prediction (NCEP) for a 6-yr period (2002–07) covering the entire CONUS between 120° and 80°W. Although stage IV has its limitations [see, e.g., Young et al. (2000) and Stellman et al. (2001) regarding the related stage III product], it does provide a more consistent representation of the relationship than does a direct comparison with gauge data since SCaMPR and stage IV are at roughly the same spatial resolution. The evaluation methodology of Tian et al. (2009) is heavily relied upon in this work as it provides a very simple framework for isolating different contributions to total error.

The overall statistics for 2002–07 are shown in Table 1. As defined in Tian et al. (2009), the hit bias is the total volume of SCaMPR rainfall minus the total volume of observed rainfall for only those pixels where rainfall was indicated by both SCaMPR and stage IV. The hit bias value and all other values have been scaled by dividing by the total observed rainfall. Table 1 indicates that the overall SCaMPR error was reduced by nearly a third by adding TRMM to the calibration dataset. This was largely driven by a significant decrease in false alarms. The percentage volume of missed rainfall was largely unchanged, while for those pixels correctly indicated by SCaMPR to be raining, SCaMPR became wetter when TRMM was added, changing a weak dry bias to an even weaker wet bias.

A closer examination of these statistics can provide information about the relative impact of the MW bias adjustment and direct TRMM data ingest on the two main components of the SCaMPR algorithm: rain/no-rain discrimination and rain rate. Changes in the volume of

TABLE 1. Performance statistics of SCaMPR without and with TRMM data in comparison with stage IV radar–gauge rainfall fields for SCaMPR for the period 2002–07 over the CONUS from 120° to 80°W. Hit refers to the hit bias—the volume of SCaMPR rainfall minus the volume of stage IV rainfall for those pixels correctly identified as raining by SCaMPR. Miss refers to the total volume of stage IV rainfall in pixels with no SCaMPR rainfall. False refers to the total volume of SCaMPR rainfall in pixels with no rain in stage IV. The total rainfall error is hit – miss + false. All amounts have been divided by the total volume of stage IV rainfall.

| Algorithm | Hit | Miss | False | Total |
|-----------|--------|-------|--------|--------|
| Control | −0.071 | 0.488 | 0.951 | 0.392 |
| with TRMM | 0.030 | 0.498 | 0.736 | 0.268 |
| % change | −57.75 | +2.05 | −22.61 | −31.63 |

missed rainfall are primarily controlled by changes in the rain/no-rain separation (assuming that the two areas of missed rainfall being compared do not have significantly different distributions), and the relatively small change in missed rainfall suggests that most of the impact on SCaMPR performance was the result of changes in the rainfall-rate retrieval.

The false alarm volume is by itself an ambiguous indicator in this regard since changes can be caused by changes in either the area of false alarm rainfall or in the volume of retrieved rainfall in false alarm pixels. This ambiguity can be at least partially resolved by separately determining the changes in the area (which is affected by rain/no-rain separation only) and the volume of the false alarm rainfall. Table 1 indicates that the total volume of false alarm rainfall decreased by 22.61% when TRMM data were added to SCaMPR, while the total area of false alarm rainfall was found to decrease by 7.97% (not shown). Since the volume decrease is 3 times the area decrease, the change in the retrieved rainfall rates can be said to be more significant than the (still nontrivial) change in the rain/no-rain separation. The relative impact on these two portions of the algorithm will be explored further in section 3b while discussing the relative impact of the MW bias adjustment and the direct ingest of TRMM rainfall rates.

b. Relative impact of MW bias adjustment and added TRMM rainfall rates

One way to separate the impact of the TMI-driven bias correction to the MW rain rates from that of adding TMI and PR to the predictor dataset is to examine spatial plots of the error statistics and their changes. Since the bias adjustment is applied equally at all latitudes whereas TRMM data are available only south of 38°N, one would expect that the effects of the bias adjustment would have little or no variation of latitude whereas the additional TRMM data would have an increasing impact from north to south as the overlapping

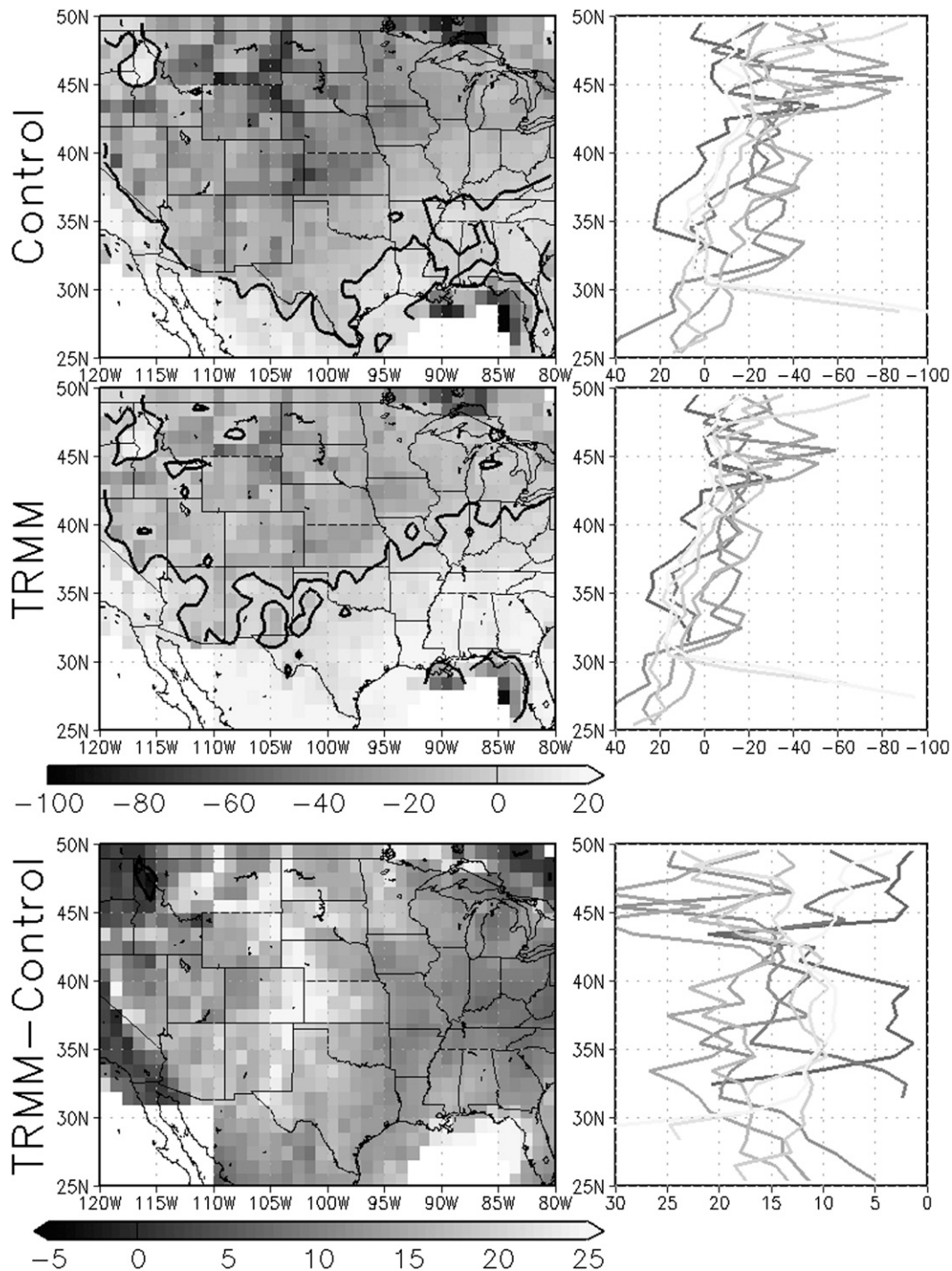


FIG. 1. Total precipitation volume of hit pixels divided by the total stage IV precipitation volume for (top) SCaMPR without TRMM and (middle) SCaMPR with TRMM, and (bottom) the difference between the two. The thick black contours indicate a value of zero. (right) South-to-north cross sections from 120° to 85°W in 5° increments, starting with darker traces to the west and lighter traces towards the east.

$15^{\circ} \times 15^{\circ}$ boxes incorporated increasing amounts of TRMM data. Therefore, latitudinal changes in the performance statistics would point to a greater impact of the added TRMM data whereas a similar impact over all

latitudes would suggest that the bias correction had the greater influence on the results.

Figure 1 is a plot of the hit bias of hourly rainfall (again, divided by the observed total) for each $1^{\circ} \times 1^{\circ}$

latitude–longitude box, where the values of each 4-km grid box within the $1^\circ \times 1^\circ$ grid box are pooled together to calculate all statistics. To the right of the spatial plots are south-to-north cross sections at 5° longitude intervals from 120° to 85°W . (The lines become lighter for cross sections farther to the east; multiple lines were plotted in place of a single longitudinally averaged series because the longitude ranges differ with latitude and hence longitudinal differences could affect the results). While there is a noticeable north–south trend in the SCaMPR hit bias in general (with a dry bias centered over the northern Rockies and a wet bias over portions of the Southeast and Southwest), there is no clear latitudinal pattern in the change in hit bias in the bottom panel of Fig. 1 or in the corresponding cross sections. This suggests that the increased wetness of “hit” pixels when TRMM data are added is primarily driven by the bias adjustment and that the addition of TMI and PR data to the target dataset has little additional impact.

It is worth noting that there is a longitudinal variation whereby the biggest increases are found in the central part of the United States and the smallest closer to the coasts, but this would not be caused by the presence or absence of TMI and PR data in the calibration data. The most likely causes of these variations are differences in subcloud evaporation of hydrometeors because of differences in low-level humidity, orographic effects in the western United States, and spatial variations in the relative proportion of stratiform and convective rainfall. Determining the precise contribution of these individual factors is beyond the scope of this paper.

The spatial distribution of missed precipitation (i.e., observed precipitation in pixels where SCaMPR indicated no precipitation) is also examined in Fig. 2. Since missed rainfall volume is a function only of the number of pixels identified as raining by the retrieval (and by the observed rainfall at those pixels), one would expect that the bias correction would have minimal impact and thus any changes observed should be the result of the addition of TRMM and PR to the target data. Indeed, while the regional variation in missed rainfall is clear, with the least missed rainfall in the plains and greater amounts of missed rainfall in the Rockies and toward the Northeast, the most significant observation is a pronounced north–south gradient in the impact of TRMM on missed rainfall in the bottom panel in Fig. 2 and in the corresponding cross section: missing rainfall decreases in many portions of the southern United States when TRMM data are added but increases with latitude. Note that the anomalous feature in parts of the Columbia River basin appears to be an artifact of the stage IV data: when a comparison is made to 24-h gauges (not shown), this feature disappears.

However, the significant increase in missed rainfall in the northernmost latitudes appears to be counterintuitive since the only effect of TRMM at those latitudes would be the bias adjustment and the MW bias adjustment should not affect the rain/no-rain separation. However, if the adjustment were to reduce the MW rain rates at the lower end of the spectrum and thus reduce the number of MW pixels defined as “raining” (i.e., with rain rates exceeding the minimum threshold), then the rain/no-rain threshold would be expected to increase and the MW bias adjustment would in fact affect the volume of missed rainfall.

This hypothesis can be tested by examining the effects of the bias adjustments on the MW rainfall rates. Figure 3a compares the adjusted SSM/I and AMSU-B/MHS rain rates to the corresponding unadjusted rain rates (showing only a dozen sample adjustments to make the plot more readable), and the close-up in Fig. 3b shows that AMSU-B/MHS rain rates as high as 5 mm h^{-1} may be adjusted below the 2 mm h^{-1} rain/no-rain threshold value for that sensor. A downward adjustment to rain rates in this range might appear counterintuitive since the AMSU-B/MHS is in theory less sensitive to light rain than the TMI, but this is consistent with Fig. 5 of Wolff and Fisher (2009) and is explained by efforts by the algorithm developers to increase sensitivity to light rain, which unintentionally led to excessive rainfall in the range of roughly $0.5\text{--}2.0 \text{ mm h}^{-1}$. This downward adjustment in AMSU rain rates is important because some pixels in the calibration dataset that would have been originally classified as raining are now considered to be nonraining, so the threshold predictor value required for a pixel to be classified as raining by SCaMPR will increase. Something similar appears to be occurring with the SSM/I for its selected rain/no-rain threshold of 0.25 mm h^{-1} —a downward adjustment that also appears to be consistent with Fig. 5 in Wolff and Fisher (2009).

That this had the hypothesized impact on the rain/no-rain separation equations can be confirmed by examining the rain/no-rain separation equations for the most frequently selected predictor in the SCaMPR regions outside the TRMM coverage area, which would be the northernmost tier of $15^\circ \times 15^\circ$ boxes that cover $35^\circ\text{--}50^\circ\text{N}$ and $120^\circ\text{--}80^\circ\text{W}$. The most frequently selected predictor pair for rain/no-rain discrimination is $T_{10.7}$ and $T_{6.7}$, and G_t and S , and the average rain/no-rain equation for that predictor pair (determined by averaging the coefficients across the entire time period for the northernmost tier of $15^\circ \times 15^\circ$ boxes) is plotted in Fig. 4a (the average was plotted instead of all of the individual equations because the scatter among all of the individual equations makes the impact of the TRMM data more difficult to distinguish). Keeping in mind that the area of rain is above

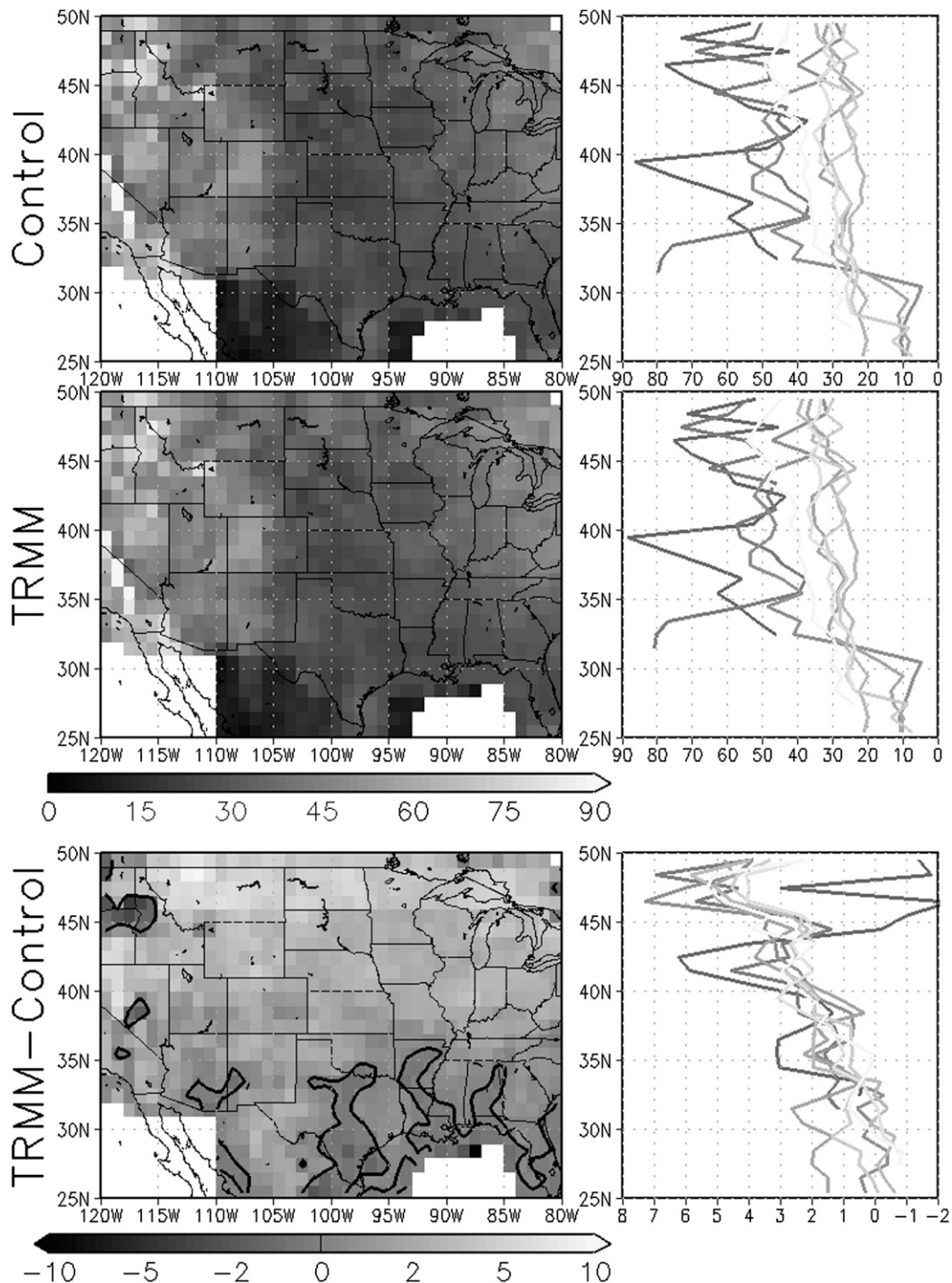


FIG. 2. As in Fig. 1, but for missed precipitation divided by the total stage IV precipitation volume.

(the higher G_r - S pair indicates more textured cloud that is more likely to be convective) and to the left (the lower $T_{10.7}$ - $T_{6.7}$ pair also indicates that the cloud is more likely to be convective), there is a slight displacement of the rain/no-rain discrimination line consistent with a smaller

number of raining pixels being detected. This supports the hypothesis that the bias adjustment with TRMM reduced the MW rain rates at low values so that fewer pixels exceeded the rain/no-rain threshold and thus the rain/no-rain threshold for SCA-MPR was made more

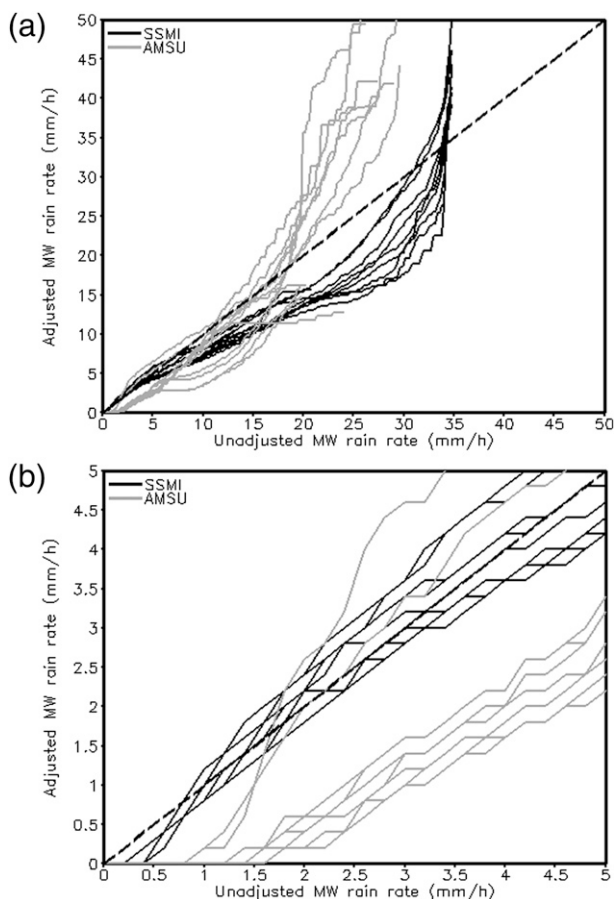


FIG. 3. Adjustment of MW rain rates to match the TMI distribution for several sample cases—15 Jan, 15 Apr, 14 Jul, and 12 Oct 2003, 2005, and 2007—for both the SSM/I (black) and AMSU-B/MHS (gray), with the thick dashed line indicating no adjustment. (a) The entire range of MW values and (b) a close-up for the 0–3 mm h⁻¹ range.

stringent. A comparison with the equivalent curves for the tier of boxes entirely within the TRMM coverage area (20°–35°N, 120°–80°W) in Fig. 4b shows that this impact was mostly cancelled out by the addition of TMI and PR data to the dataset—consistent with the generally neutral to slightly positive impact on missing rainfall in the lower latitudes exhibited in Fig. 2.

It should also be noted that Fig. 3 also explains the apparently inconsistent patterns of behavior of more rainfall retrieved in correctly raining pixels but more missed rainfall. While fewer MW pixels were classified as raining for calibration purposes because of the lowering of the lowest rain rates, the bias adjustment augmented the highest rain SSM/I rain rates (albeit while reducing the middle-range rain rates) and also augmented the AMSU-B/MHS rain rates above roughly 15 mm h⁻¹. These augmentations would presumably be as a result of beam-filling effects in these instruments, since the

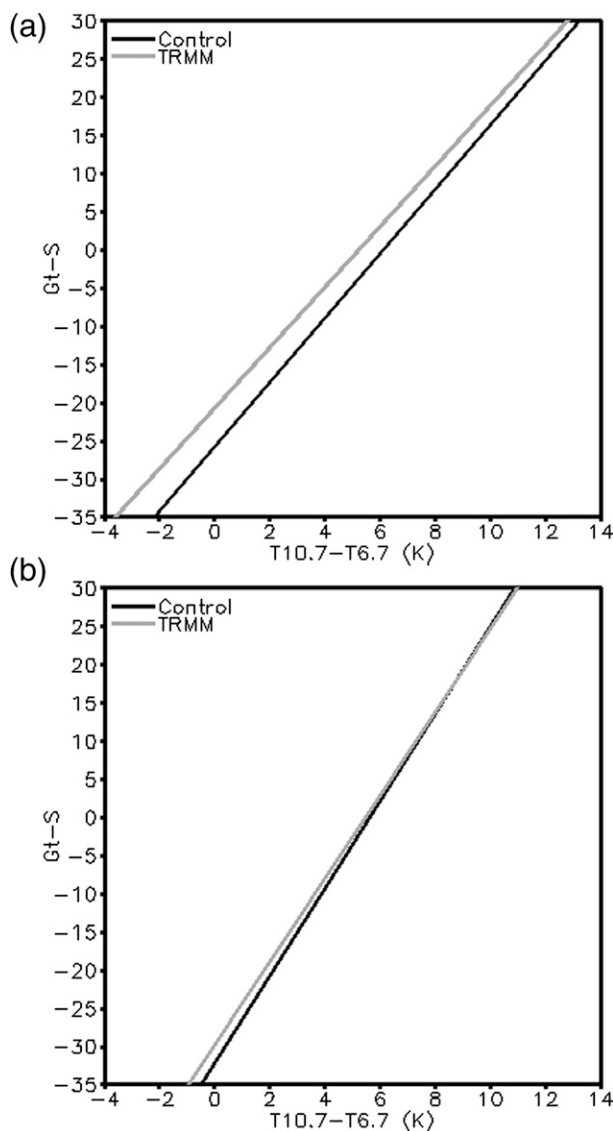


FIG. 4. Average rain/no-rain separation line in predictor space for the most frequently selected rain/no-rain predictor pair for the six SCA-MPR regions (a) north of 35°N and (b) entirely south of 35°N. The black line is the dividing line between rain (to the upper left) and no rain (to the lower right).

heaviest precipitation features only occupy part of the beam (see, e.g., Wolff and Fisher 2009).

The evidence thus far shows that the bias adjustment to the MW data has greater impact on the algorithm performance than does ingest of the TRMM data. False alarms will be examined next, with separate analyses of the false alarm volume and area to reduce ambiguity as discussed in the previous section. The spatial plots and cross sections of the false alarm volume and percentage change when adding TRMM in Fig. 5 indicate that adding the TRMM data has an impact everywhere but that

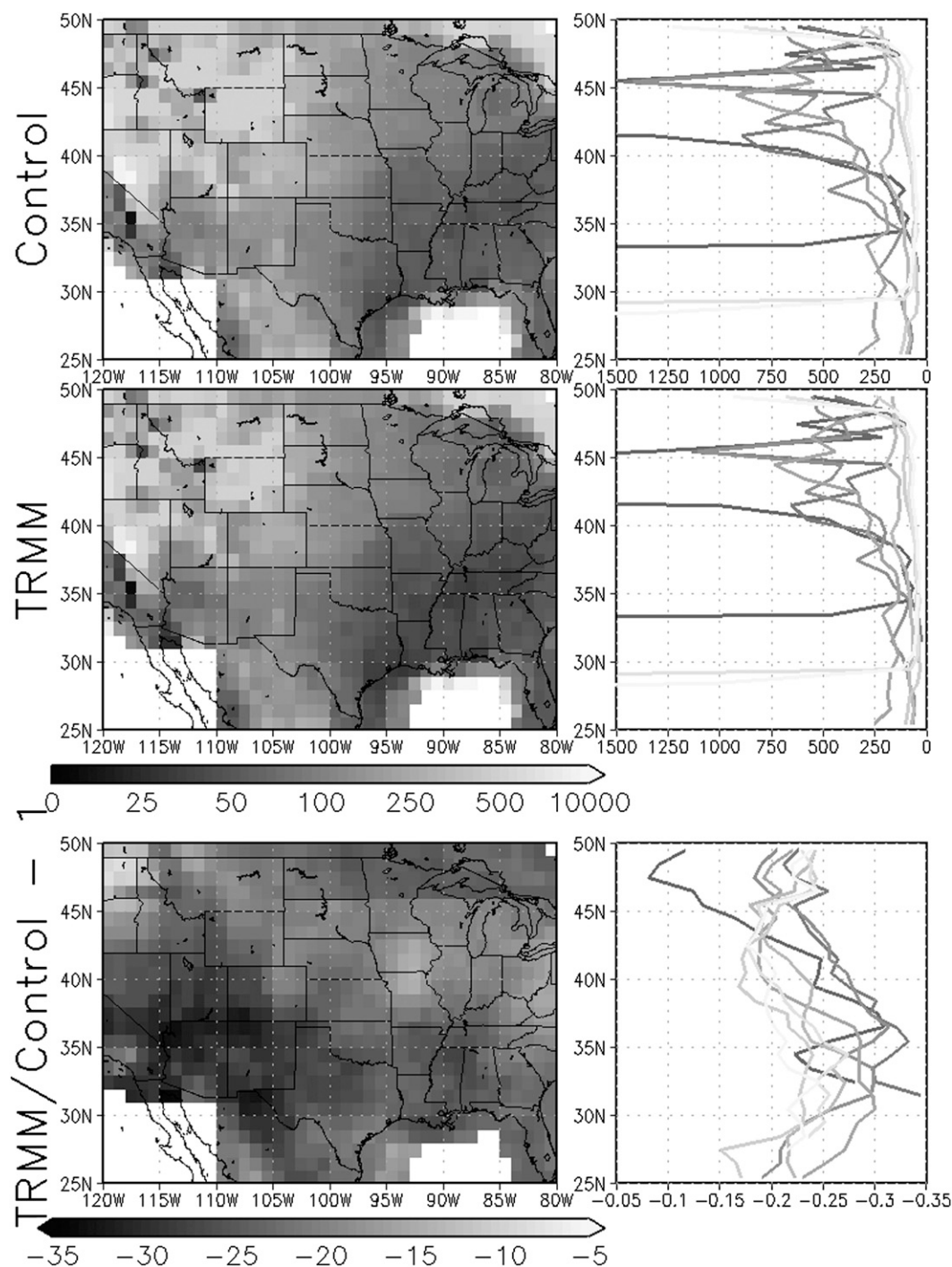


FIG. 5. As in Fig. 1, but for false alarms and with the ratio instead of the difference in the bottom panel.

a south-to-north gradient in false alarm reduction is evident with the greatest reduction south of 35°N in the TRMM coverage area. This suggests that the MW bias adjustment and the addition of the PR and TMI data are both contributing to the reduction in false alarms. Note that in this case the fractional change in false alarms is

shown in place of the differences, as in Figs. 1 and 2. This is because the strong west-to-east gradient in false alarms produces a similar west-to-east gradient when the differences are considered: the magnitude of the changes is greater in the west than in the east because the original magnitude of the false alarms is much higher.

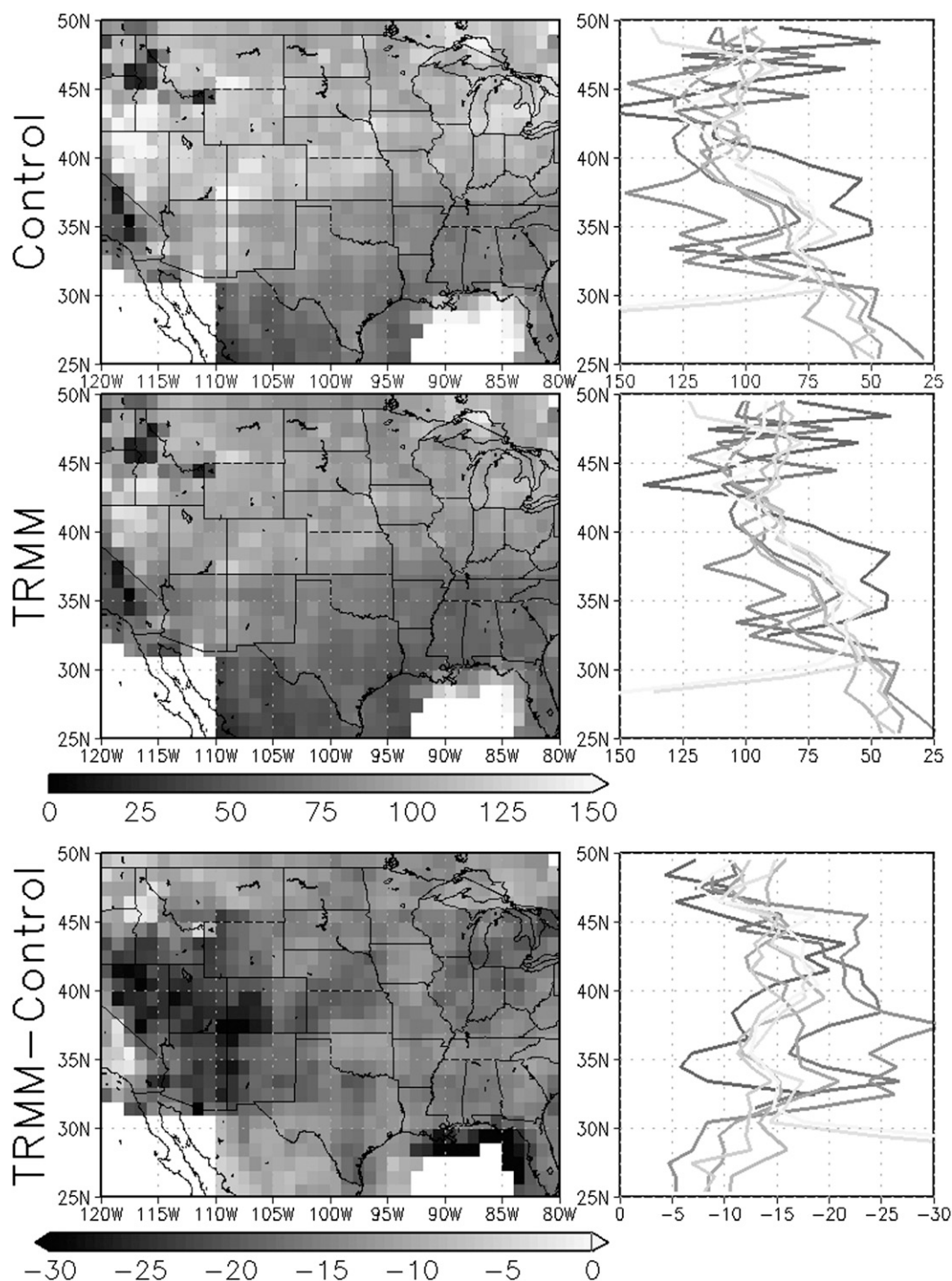


FIG. 6. As in Fig. 1, but all values are divided by the number of false alarm pixels and then divided by the number of observed raining pixels to get the false alarm volume per false alarm pixel.

The spatial plot and cross section of the normalized volume of false alarms divided by the normalized area of false alarms in Fig. 6 are obtained by simply dividing the values in Fig. 5 by the number of false alarm pixels divided by the number of observed raining pixels. The plot

shows a general south-to-north gradient of increasing volume of rainfall in false alarm pixels, but no consistent gradient in the reduction in false alarm volume per pixel when TRMM is added. This suggests that the impact of the directly ingested TRMM data is mainly in reducing

the number of false alarm pixels and that it does not have a significant effect on reducing the volume of rainfall in pixels incorrectly identified as raining.

In the absence of impact of the directly ingested TRMM data on reducing false alarms, the reduction of false alarm area by the MW bias adjustment is explained by the mechanism that reduced correct detections: the distribution adjustment reduced the number of raining pixels in the training dataset, raising the rain/no-rain threshold during training and thus reducing the number of pixels classified as raining. However, the reduction in false alarms was much greater than the increase in missed rainfall, indicating that the changes in the rain/no-rain calibration in SCaMPR from adding TRMM data generally were skillful.

In summary, the addition of TRMM data to SCaMPR moistens those pixels where SCaMPR correctly detects rainfall, turning a dry bias into a slight wet bias. Adjusting the MW rain rates to match the TMI distribution raises the rain detection threshold values and thus causes slightly more missed rainfall but significantly less false alarm rainfall. The direct ingest of the TRMM data partially counteracts the increase in missed rainfall but appears to have no other significant effects. Interestingly, adding TRMM data to SCaMPR (correctly) increases rain rates for correctly identified raining pixels (Fig. 1) but also (correctly) reduces them for pixels incorrectly identified as raining (Fig. 5). This would appear to indicate that the changes in the rain-rate equations introduced by bias adjusting the MW rainfall rates improve skill and do not indiscriminately increase rainfall rates under all circumstances.

One potential caveat regarding this analysis is that SCaMPR combines land and ocean MW pixels in the training dataset, so spatial variations in the relative fraction of land and (more accurate) ocean MW retrievals in the training data could conceivably explain some of the observed variations. However, the impact would be expected to be rather small since changes in the land-ocean fraction in the training data would occur only if a TRMM ocean footprint replaced an AMSU-B/MHS footprint in the training data. Evidence of such an impact could conceivably be found in longitudinal variations in the difference statistics for the southern portions of the analysis area, with a peak or trough expected around 105°W where the land fraction is highest. However, while Fig. 1 shows some signs of such a feature, Figs. 2 and 5–6 do not, implying that the latitudinal variations that are observed are not being significantly influenced by land-ocean effects.

c. Error budget

An important question is how much of the error in the SCaMPR rainfall-rate estimates is contributed by the

TABLE 2. Performance statistics for the SSM/I and AMSU-B/MHS before and after adjusting to match the distribution of the TMI rain rates.

| | Hit bias (%) | Miss (%) | False (%) | Total (%) |
|---------------------|--------------|----------|-----------|-----------|
| SSM/I | −31.2 | 23.8 | 69.8 | 14.8 |
| Adjusted SSM/I | −14.7 | 26.0 | 60.1 | 19.4 |
| AMSU-B/MHS | −28.8 | 33.0 | 64.5 | 2.7 |
| Adjusted AMSU-B/MHS | −3.2 | 41.9 | 26.5 | −18.6 |

errors in the MW rain rates (the calibration source) versus deficiencies in the algorithm (the calibration process). Comparing the results for the control and TRMM versions of SCaMPR also provides a secondary measure of the relative impact of the MW rain-rate calibration adjustment versus the addition of the TMI and PR rain rates to the algorithm. To minimize the effects of spatial resolution differences, the instantaneous SCaMPR rainfall rates and the stage IV 1-h rainfall amounts were mapped using spatial aggregation onto the corresponding 15-km SSM/I or AMSU-B/MHS pixels or the corresponding 5-km TMI pixels for comparison. There is some uncertainty introduced by comparing the instantaneous SCaMPR and MW rain rates with 1-h stage IV totals (unlike the previous section where 1-h SCaMPR totals were compared to 1-h stage IV totals), but since the relative performance rather than the absolute performance is being considered, it is assumed that these errors affect the SCaMPR and MW data similarly.

Table 2 shows the error components for the SSM/I and AMSU-B/MHS before and after being adjusted to match the TMI distribution; in this case, a rain/no-rain threshold of 0.5 mm h^{−1} was used for the SSM/I and 2 mm h^{−1} for the AMSU-B/MHS. In both cases, the hit bias goes from being strongly negative to weakly negative (being nearly eliminated in the AMSU-B/MHS), while misses increase slightly and false alarms decrease slightly for the SSM/I but more significantly for the AMSU-B/MHS. This is consistent with the earlier observation that the bias adjustment (see Fig. 3) lowered many AMSU-B/MHS and SSM/I rain rates at the low end of the distribution (thus decreasing false alarms) but raised the rates at the high end of the spectrum, thus moistening those pixels that correctly depicted rainfall. The stronger moistening for the AMSU-B/MHS versus the SSM/I pixels in Table 2 is also supported by Fig. 3, as the AMSU-B/MHS has moistening over a much wider range of values than does the SSM/I.

It is worth noting that this case illustrates the importance of examining the individual components of error and not the just the overall error. The total error (fourth column in Table 2), which is the hit bias plus the false

TABLE 3. Statistical comparison of matched MW and (aggregated) SCaMPR pixels against (aggregated) stage IV values for 2002–07.

| | Hit bias (%) | Miss (%) | False (%) | Total (%) |
|----------------------|--------------|----------|-----------|-----------|
| Unadjusted MW | −30.2 | 27.8 | 67.6 | 9.6 |
| SCaMPR-no TRMM | −13.9 | 48.9 | 118.2 | 55.4 |
| MW % of SCaMPR error | — | 56.9 | 57.2 | — |
| Adjusted MW | −7.8 | 28.3 | 43.8 | 7.7 |
| SCaMPR-TRMM | −1.2 | 46.3 | 84.2 | 36.3 |
| MW % of SCaMPR error | — | 61.1 | 52.0 | — |

alarms minus the missed rainfall, actually increases despite significant reductions in two of the three error components. The increase in missed rainfall does account for approximately half of the increase in total error, but the large reduction in hit bias by the error adjustment means that less of the false alarm error is canceled out, and so the total error actually increases even though the false alarm error has also decreased.

Table 3 compares the errors in both versions of SCaMPR (with and without the TRMM data) with the errors in the corresponding MW pixels from their respective training datasets to provide a measure of the contribution of the MW error to the overall SCaMPR error. This was done by aggregating the SCaMPR output onto the MW footprints for the same time and location to enable a direct comparison with stage IV data, which has also been aggregated onto the MW footprint. Strictly speaking, since SCaMPR retrievals are performed on independent IR data, the MW rain rates to which the SCaMPR retrievals are being compared were not part of the training data, so it is assumed that the error characteristics of the MW rain rates do not change significantly over the time elapsed between the SCaMPR training data and the independent data. There are also some errors in comparing the instantaneous SCaMPR and MW rainfall rates with 1-h totals from stage IV, but assuming the resulting sampling errors are roughly the same for both algorithms, the comparison is valid.

When compared directly, in both cases the magnitudes of the MW errors are roughly 60% of the magnitudes of the corresponding SCaMPR errors, implying that somewhat more than half of the missed rainfall and false alarms in SCaMPR are attributable to the MW calibration data. From a different perspective, the approximation of the MW rainfall rates using IR data in SCaMPR nearly doubles the amount of missed rainfall and false alarm rainfall. This should not be surprising since the IR brightness temperatures are sensitive only to cloud-top properties whereas the MW data are sensitive to bulk cloud properties; one should not expect the former to entirely replicate the information content of

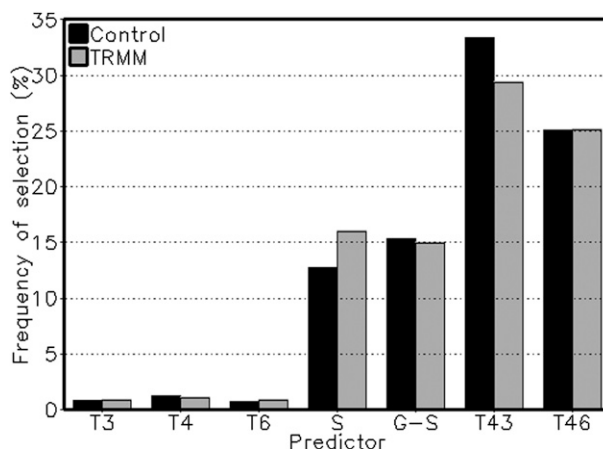


FIG. 7. Frequency of selection of the available rain/no-rain SCaMPR predictors.

the latter. Since a reduction in SCaMPR error to the level of TRMM error is thus not a reasonable expectation, it is difficult to determine objectively how well this approach has optimized the use of the TRMM data in SCaMPR, and future work may be able to achieve additional improvements from ingesting the TRMM data.

However, the increase false alarms and missed rainfall from attempting to approximate the MW rain rates using IR data is compensated for to a degree by a significantly lower negative hit bias in SCaMPR compared to the input MW data. It is not immediately clear why this should occur given that SCaMPR is being calibrated against the MW data and theoretically should not be able to outperform it. One possible explanation is that linear regression assumes normally distributed data and that the application of regression to a highly skewed distribution like rainfall rate may induce wet biases—this would also explain the significant increase in false alarm rainfall in SCaMPR versus the input MW rainfall rates.

d. Effects on SCaMPR predictor selection

Another important question concerns whether the addition of the TRMM data had any material effect on the predictors selected by SCaMPR; that is, did the relationship between the MW rainfall areas and/or rates to the GOES predictors change significantly when TRMM data were used to bias adjust the MW data and were also added to the predictor data? Figure 7 shows the frequency of selection among the seven candidate SCaMPR rain/no-rain predictors (the selections as a first or second predictor are combined here) for both the control and TRMM versions of SCaMPR. For both runs the brightness temperature values for individual bands are nearly never selected, but there is some change in that the

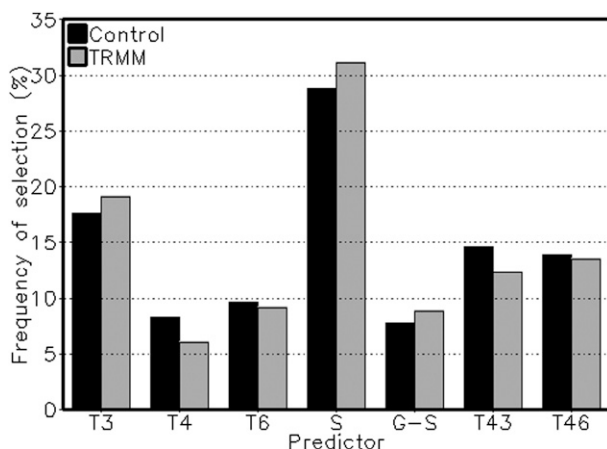


FIG. 8. As in Fig. 7, but for the available rain-rate SCaMPR predictors.

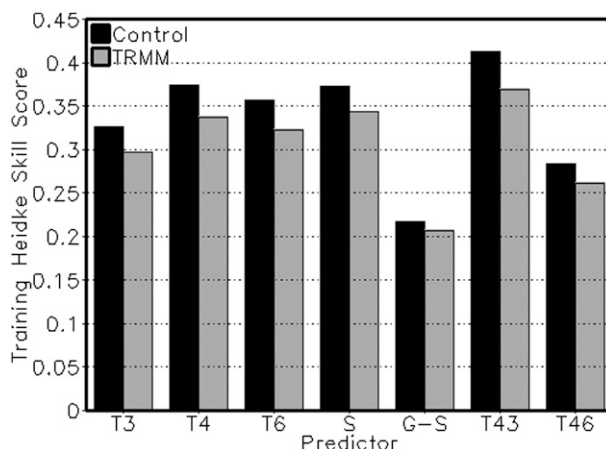


FIG. 9. Average HSS of the SCaMPR rain/no-rain predictors for 2002–07.

TRMM version of SCaMPR favors the brightness temperature difference between 10.7 and 6.7 μm a bit less than the control version (29.3% vs 33.3%), and most of this difference is made up by an increase in the favoring of S (16.0% vs 12.6%). Since these are the only two predictors experiencing significant changes, it would appear that a number of the cases, where the $T_{10.7}$ – $T_{6.7}$ pair is used, are switching to using S for rain/no-rain discrimination, but the reason for this is not obvious.

The corresponding frequency of selection for the rain-rate predictors (where the linear and nonlinear versions are combined and the first and second predictors are combined) is shown in Fig. 8. The most frequently selected predictor is S , which is not surprising since it is effectively an expression of the minimum value of $T_{10.7}$ in the 5×5 pixel neighborhood, which is much less sensitive to mismatches between the coldest cloud tops and heaviest rain rates than the $T_{10.7}$ values. The selection of $T_{6.7}$ with the second-greatest frequency is somewhat surprising but consistent with previous findings (Kuligowski 2002) and may also be because the field is generally somewhat smoother than $T_{10.7}$ and thus may be less sensitive to location errors.

As far as differences between the control and TRMM runs, there are numerous small changes, particularly slight increases in the frequency of selection of S (28.7%–31.1%) and $T_{6.7}$ (17.5%–19.1%) and corresponding decreases in the frequency of selection of the $T_{10.7}$ – $T_{6.7}$ pair (14.5%–12.3%) and $T_{10.7}$ (8.2%–6.1%), but determining the relationship among these changes would require a case-by-case analysis.

One would expect these changes to be related to changes in the relative skill of the predictors; for example, if S is chosen more frequently at the expense of the $T_{10.7}$ – $T_{6.7}$

pair for rain/no-rain discrimination, it would appear to follow that the skill of S increased relative to the skill of the $T_{10.7}$ – $T_{6.7}$ pair at discriminating raining from non-raining pixels. However, the HSS values of each predictor in both runs decreased almost uniformly (with little change in relative value) when the TRMM data were added (Fig. 9), and so the reasons for the change would need to be found via a case-by-case examination. The same is true for the correlation coefficient of the rainfall-rate predictors (not shown). Although this would appear to imply at first blush that the TRMM data actually degraded the data sample, it should be kept in mind that the performance on independent data improved when TRMM data were added, implying that the calibration derived with TRMM data were more robust than those without, even if the traditional measures of goodness of fit implied slight degradation.

4. Conclusions and future work

The application of TRMM data to short-term hydrologic forecasting is difficult to do directly because of infrequent sampling and data latency. However, incorporating TRMM data into a multisensor framework for short-fuse satellite rainfall estimates provides an opportunity to evaluate their potential utility. Toward this end, experiments were performed with ingesting TRMM data into the SCaMPR framework for the period 2000–07, and the output for the last 6 yr of that record were compared to hourly stage IV radar–gauge data to evaluate the impact of the data.

The primary findings were that TRMM data indeed had a positive impact on the performance of SCaMPR, primarily by addressing a dry bias in pixels that were correctly classified as raining by the algorithm and by

reducing both the occurrence and (especially) the volume of false alarm rainfall. Having TRMM data coverage over only a portion of the CONUS evaluation area provided the opportunity to distinguish impacts from bias adjusting the MW data prior to ingest and directly using TMI and PR data in the calibration dataset, and it was found that the impacts of bias adjustment significantly outweighed the impacts of using the TMI and PR data directly in the calibration data. However, there were generally six combined SSM/I and AMSU-B/MHS instruments providing data compared to a single TMI or PR, and given the difference in swath width between the two, the TMI and PR would have represented perhaps 10% of the total calibration data volume. Hence, it is not surprising that the impact was relatively muted. Similarly in the GPM era, one would expect that for this particular application the calibration of rain rates from the other satellites in the GPM constellation to match those from the GPM core satellite will have a greater impact than just the additional data provided by the core satellite itself.

It should be noted that the conclusions presented herein appear to be different from the analysis in Zhang et al. (2013): that paper noted that ingesting TRMM into SCaMPR mitigated the positive overall bias but elevated the false alarm rate. However, in that paper the bias referred to all pixels (hits, misses, and false alarms), and the total error (bias) in Table 1 shows that the overall bias was indeed reduced, with a strong reduction in false alarms (which will contribute to an overall wet bias) more than compensating for the increased rainfall in “hit” pixels that were previously too dry. Regarding the false alarm rate, Zhang et al. (2013) focus on false alarm rates for the heaviest 3%, 1%, and 0.1% (i.e., most hydrologically significant) rainfall events, whereas the analysis presented here accounts for all rainfall events regardless of intensity. The false alarm behavior and overall skill of SCaMPR (and other rainfall algorithms) vary as a function of rainfall intensity.

In response to these findings, the real-time version of SCaMPR was modified to include TRMM data both to bias correct the other satellites and as a source of calibration data. Since a blended, bias-corrected dataset is already operationally available from the CPC, the microwave combined (MWCOMB) product (Joyce and Xie 2011) is being used instead of performing the data ingest and calibration in real time. This same dataset is also being used as the calibration source for the upcoming GOES-R rainfall-rate algorithm, which will be discussed in a future paper.

As a final note, it should be kept in mind that the error of the SCaMPR algorithm will always be dependent on the error in the calibration MW dataset; since SCaMPR

is calibrated using MW rain rates, it cannot in general outperform them. However, this is not necessarily problematic since the objective of this approach is not to compete directly with MW rain rates but to extend their application to latency times that are significantly shorter than those for data used directly from polar-orbiting instruments. In addition, corrections for factors not addressed in the MW algorithms such as orographic modulation of rainfall and subcloud evaporation of hydrometeors can be accounted for by SCaMPR, and this will be the subject of a future paper.

Acknowledgments. This work was supported by the NOAA/NESDIS/Office of Satellite Products and Operations (OSPO) GOES I-M Product Assurance Plan (GIMPAP), the GOES-R Program Office Risk Reduction Program, and the NOAA/NESDIS/Office of Systems Development via support for a NASA Precipitation Measurement Missions (PMM) project. Three anonymous reviewers provided valuable feedback that significantly improved the manuscript. The contents of this paper are solely the opinions of the authors and do not constitute a statement of policy, decision, or position on behalf of NOAA or the U.S. government.

REFERENCES

- Adler, R. F., and A. J. Negri, 1988: A satellite infrared technique to estimate tropical convective and stratiform rainfall. *J. Appl. Meteor.*, **27**, 30–51.
- Ba, M. B., and A. Gruber, 2001: GOES multispectral rainfall algorithm (GMSRA). *J. Appl. Meteor.*, **40**, 1500–1514.
- Bellerby, T., M. Todd, D. Kniveton, and C. Kidd, 2000: Rainfall estimation from a combination of TRMM precipitation radar and GOES multispectral satellite imagery through the use of an artificial neural network. *J. Appl. Meteor.*, **39**, 2115–2128.
- Ebert, E. E., J. E. Janowiak, and C. Kidd, 2007: Comparison of near-real-time precipitation estimates from satellite observations and numerical models. *Bull. Amer. Meteor. Soc.*, **88**, 47–64.
- Ferraro, R. R., 1997: SSM/I derived global rainfall estimates for climatological applications. *J. Geophys. Res.*, **102**, 16 715–16 735.
- , and Coauthors, 2005: NOAA operational hydrological products derived from the Advanced Microwave Sounding Unit. *IEEE Trans. Geosci. Remote Sens.*, **43**, 1036–1049.
- Hong, Y. A., K.-L. Hsu, S. Sorooshian, and X. Gao, 2004: Precipitation estimation from remotely sensed imagery using an artificial neural network cloud classification system. *J. Appl. Meteor.*, **43**, 1834–1852.
- Hsu, K.-L., X. Gao, S. Sorooshian, and H. V. Gupta, 1997: Precipitation estimation from remotely sensed information using artificial neural networks. *J. Appl. Meteor.*, **36**, 1176–1190.
- Huffman, G. J., and Coauthors, 2007: The TRMM Multisatellite Precipitation Analysis (TMPA): Quasi-global, multiyear, combined-sensor precipitation estimates at fine scales. *J. Hydrometeorol.*, **8**, 38–55.
- Iguchi, T., T. Kozu, J. Kwiatkowski, R. Meneghini, J. Awaka, and K. Okamoto, 2009: Uncertainties in the rain profiling algorithm

- for the TRMM precipitation radar. *J. Meteor. Soc. Japan*, **87A**, 1–30.
- Joyce, R. J., and P. Xie, 2011: Kalman filter-based CMORPH. *J. Hydrometeorol.*, **12**, 1547–1563.
- Kuligowski, R. J., 2002: A self-calibrating GOES rainfall algorithm for short-term rainfall estimates. *J. Hydrometeorol.*, **3**, 112–130.
- Kummerow, C., and Coauthors, 2001: The evolution of the Goddard profiling algorithm (GPROF) for rainfall estimation from passive microwave sensors. *J. Appl. Meteor.*, **40**, 1801–1820.
- Lin, Y., and K. E. Mitchell, 2005: The NCEP stage II/IV hourly precipitation analyses: Development and applications. Preprints, *19th. Conf. on Hydrology*, San Diego, CA, Amer. Meteor. Soc., 1.2. [Available online at <https://ams.confex.com/ams/pdfpapers/88063.pdf>.]
- McCollum, J., and R. Ferraro, 2003: Next generation of NOAA/NESDIS TMI, SSM/I, and AMSR-E microwave land rainfall algorithms. *J. Geophys. Res.*, **108**, 8382, doi:10.1029/2001JD001512.
- Miller, S. W., P. A. Arkin, and J. Royce, 2001: A combined microwave/infrared rain rate algorithm. *Int. J. Remote Sens.*, **22**, 3285–3307.
- Scofield, R. A., 2001: Comments on “A quantitative assessment of the NESDIS Auto-Estimator.” *Wea. Forecasting*, **16**, 277–278.
- Stellman, K. M., H. E. Fuelberg, R. Garza, and M. Mullusky, 2001: An examination of radar and rain gauge-derived mean areal precipitation over Georgia watersheds. *Wea. Forecasting*, **16**, 133–144.
- Tian, Y., and Coauthors, 2009: Component analysis of errors in satellite-based precipitation estimates. *J. Geophys. Res.*, **114**, D24101, doi:10.1029/2009JD011949.
- Turk, F. J., E. E. Ebert, H. J. Oh, B.-J. Sohn, V. Levizzani, E. A. Smith, and R. Ferraro, 2003: Validation of an operational global precipitation analysis at short time scales. Preprints, *Third Conf. on Artificial Intelligence/12th Conf. on Satellite Meteorology and Oceanography*, Long Beach, CA, Amer. Meteor. Soc., JP1.2. [Available online at <https://ams.confex.com/ams/pdfpapers/56865.pdf>.]
- Ushio, T., and Coauthors, 2009: A Kalman filter approach to the Global Satellite Mapping of Precipitation (GSMaP) from combined passive microwave and infrared radiometric data. *J. Meteor. Soc. Japan*, **87A**, 137–151.
- Vicente, G. A., R. A. Scofield, and W. P. Menzel, 1998: The operational GOES infrared rainfall estimation technique. *Bull. Amer. Meteor. Soc.*, **79**, 1883–1898.
- , J. C. Davenport, and R. A. Scofield, 2002: The role of orographic and parallax corrections on real time high resolution satellite rain rate distribution. *Int. J. Remote Sens.*, **23**, 221–230.
- Vila, D., R. Ferraro, and R. Joyce, 2007: Evaluation and improvement of AMSU precipitation retrievals. *J. Geophys. Res.*, **112**, D20119, doi:10.1029/2007JD008617.
- Wolff, D. B., and B. L. Fisher, 2009: Assessing the relative performance of microwave-based satellite rain-rate retrievals using TRMM ground validation data. *J. Appl. Meteor. Climatol.*, **48**, 1069–1099.
- Young, C. B., A. A. Bradley, W. F. Krajewski, and A. Kruger, 2000: Evaluating NEXRAD multisensor precipitation estimates for operational hydrologic forecasting. *J. Hydrometeorol.*, **1**, 241–254.
- Zhang, Y., D.-J. Seo, D. Kitzmiller, H. Lee, R. J. Kuligowski, D. Kim, and C. R. Kondragunta, 2013: Comparative strengths of SCaMPR satellite QPEs with and without TRMM ingest vs. gridded gauge-only analyses. *J. Hydrometeorol.*, **14**, 153–170.